Efficient Wide-Band Large-Angle Refraction and Splitting of a Terahertz Beam by Low-Index 3D-Printed Bilayer Metagratings

Xipu Dong,[1] Jierong Cheng ⓘ,[1,2,*] Fei Fan,[1] Xianghui Wang,[1] and Shengjiang Chang[1,3]

[1]*Institute of Modern Optics, Nankai University, Tianjin 300350, China*
[2]*Tianjin Key Laboratory of Micro-scale Optical Information Science and Technology, Tianjin 300350, China*
[3]*Tianjin Key Laboratory of Optoelectronic Sensor and Sensing Network Technology, Tianjin 300350, China*

Near-perfect anomalous reflection and refraction have been demonstrated using passive lossless metasurfaces and metagratings operating at microwave, infrared, and visible frequencies, while related studies at terahertz frequencies are lacking. Here we propose low-index (with a refractive index of 1.57) 3D-printed dielectric metagratings for efficient wide-band diffraction engineering at low terahertz frequencies. A simplified analytical model reveals that the number of propagating waveguide modes inside the grating is a key factor in diffraction engineering, and is insufficient in a low-index design regardless of the detailed dimensions in a period. Additional waveguide modes are introduced in asymmetric bilayer and trilayer metagratings, providing sufficient degrees of freedom for efficient large-angle anomalous refraction and beam splitting. These metagratings are inherently wide-band, benefiting from low dispersion of the waveguide modes. Three metagratings are designed, 3D printed, and tested experimentally at 0.14 THz for 70° refraction, 80° refraction, and ±70° beam splitting. The measured efficiency shows good agreement with the design. The proposed metagratings, with simple structures and large feature sizes, can be easily scaled to applications at higher terahertz frequencies.

I. INTRODUCTION

Metasurfaces, composed of a thin layer of artificially devised elements with subwavelength size and a dense lattice distribution [1,2], have been developed to provide a powerful boundary to control the direction of a beam following a generalized Snell's law [3–5]. However, it is recognized that such local phase compensation is always accompanied by parasitic scattering due to an impedance mismatch between the incoming and target beams [6]. When the transmission (reflection) direction deviates by a large amount from the incident (specular-reflection) direction, namely when one has large-angle anomalous refraction (reflection), an increased impedance mismatch leads to inefficiency. Perfect beam deflection generally requires metasurfaces to be implemented with undesired active elements [7,8], which complicates the design and fabrication. Hence, tremendous efforts are being dedicated to achieving full beam control via passive lossless metasurfaces.

Near-perfect large-angle reflection has been achieved passively by exploiting the nonlocal effects of evanescent [9,10] and leaky [11,12] modes. These evanescent and leaky modes absorb energy in one place and release it elsewhere so as to emulate gain and loss, while the

average power over a macroperiod remains constant. An alternative method of reflection manipulation is achieved by using a conformal metasurface following a power-conserved profile in order to avoid nonlocality [13]. On the other hand, reflectionless large-angle refraction can be achieved with an omega-type bianisotropic metasurface [14,15], which features magnetoelectric coupling and simultaneously matches the input and output waves via an asymmetric stack of impedance sheets.

Such layered impedance sheets have recently been fabricated in printed-circuit-board (PCB) structures [16,17]. Experimental results demonstrate efficient and reflectionless large-angle refraction around 20 GHz. Still, part of the energy is absorbed due to loss in the material. The constituent elements are chosen based on their responses in a periodic array, and then are gathered together densely to capture the fast-varying impedance profile. The intercoupling between adjacent elements is not accounted for accurately [18]. Collective optimization of all the elements is usually needed in order to approach the theoretical efficiency in practice [16,19].

Instead of implementing a rigorous surface-impedance or polarizability profile with dense scatterers, the concept of a metagrating offers an alternative solution to the problem of controlling the beam direction by concentrating energy into one or a few nonzero diffraction orders [20].

---

*chengjr@nankai.edu.cn

The scatterers in metagratings do not explicitly implement an impedance profile and therefore are not limited to a subwavelength scale and a dense distribution. Accordingly, the merits of metagratings reside in relaxed fabrication requirements and simplified design. For large-angle reflection, only two or three diffraction Bloch modes fall inside the propagation region. The use of one or two scatterers in a period backed by a ground plane has been proposed in order to send the beam into a specific diffraction order while annihilating the rest [21–24]. A metallic grating with etched uniform grooves has been proposed in order to achieve wide-band and wide-angle reflection control [25]. We have also successfully demonstrated large-angle reflection of a terahertz beam with low-index dielectric metagratings [26,27]. The concept has been generalized further to arbitrary control of n diffraction orders with enough degrees of freedom [28,29].

For large-angle refraction, a metagrating has to cancel undesired diffraction on both the transmission and the reflection side. This has been achieved at 20 GHz using layered and laterally offset PCB conducting strips, with an efficiency of 90% [30,31]. For operation in the visible and infrared bands, large-angle-refracting metagratings are usually composed of optimized high-index dielectric scatterers. TiO$_2$ [32] and Si [33] periodic dimers have been used to diffract visible light by more than 80° with an experimental efficiency of 40%. Si free-form scatterers [34] and Si bianisotropic scatterers [35] have achieved 75° beam refraction in the near IR and mid-IR with experimental efficiencies of 75% and 95%. A TiO$_2$ kissing-dimer metagrating for broadband directional scattering has also been demonstrated [36]. These all benefit from a highly asymmetric radiation pattern and multiresonance features.

Until now, large-angle refraction at terahertz (THz) frequencies has rarely been reported, except for a simulated design for trilayer metasurfaces operating at 1 THz [19]. Cascaded PCB metasurfaces operating at millimeter frequencies may be pushed up to THz operation [37,38]. In addition, there are many THz-transparent polymers [polystyrene, polyethylene, polypropylene, polylactic acid (PLA), etc.] with a relatively low refractive index of 1.5–1.6 [39–41]. They have very low absorption coefficients, especially at sub-THz frequencies (0.1–0.3 THz). The booming three-dimensional (3D) printing technique can shape such polymers into complicated structures [42, 43]. Instead of scaling PCB structures from the microwave range and scaling high-index designs from the visible range, developing low-index 3D-printed metagratings is well suited for filling the gap in the THz diffraction elements that are urgently needed for THz spectral-analysis and imaging applications [44–46]. Here we focus on achieving efficient wide-band large-angle refraction and beam splitting at THz frequencies with 3D-printed polymer metagratings.

We develop a simple analytical model to characterize diffraction in dielectric metagratings by expressing the fields in each layer via a few propagating Bloch modes. This model provides physical insights into the degrees of freedom in diffraction engineering, which are limited mainly by the number of waveguide modes in the grating layer. We next show that the number of waveguide modes is governed by the refractive index rather than the geometry of the metagrating. There are not enough waveguide modes in low-index (polymer) metagratings no matter how the constituent scatterers are designed, leading to very inefficient diffraction engineering at THz frequencies. Bilayer and trilayer gratings are then proposed, to enrich the waveguide modes and to achieve efficient and near-perfect large-angle refraction and beam splitting. Such metagratings, with a very sparse scatterer distribution (one ridge per period per layer), are 3D printed and tested at 0.14 THz; they have high efficiency and a series of additional merits, such as a large feature size, low cost, fast fabrication, and a simple design process. The simulated bandwidth is much wider than that in reported results.

II. ANALYTICAL MODEL FOR DIFFRACTION ENGINEERING WITH DIELECTRIC METAGRATINGS

As shown in Fig. 1(a), we aim to control the beam direction by concentrating the energy into one or a few specific diffraction channels of the dielectric metagrating, while suppressing spurious diffraction in other channels. One functionality that a metagrating may have is anomalous refraction, similar to that of a blazed grating. The grating period Λ is related to the refraction angle θ_t by the well-known Floquet theorem [47,48],

$$\sin(\theta_t) - \sin(\theta_i) = l\frac{\lambda}{\Lambda}, \tag{1}$$

where λ is the operation wavelength and l is the diffraction order. Normal excitation ($\theta_i = 0$) with a TM polarization (x-polarized) is considered throughout this paper, but the analysis can be extended to oblique excitation and TE polarizations. The zeroth order corresponds to normal refraction. One can choose the period so that the anomalous refraction matches the next diffraction order, with $l = 1$, leading to a grating period $\Lambda = \lambda/\sin\theta_t$ with a few ridges included [there are two ridges per period in Fig. 1(b)]. When $\theta_t > 30°$, Eq. (1) implies that only three propagating diffraction channels ($l = 0, \pm1$) exist, on both the transmission and the reflection side, with the higher-order diffraction being evanescent. Hence, one needs to block five channels to efficiently guide energy into the first order in transmission, as shown in Fig. 1(a). For small-angle anomalous refraction with $\theta_t < 30°$, the complexity of the metagrating design increases as more
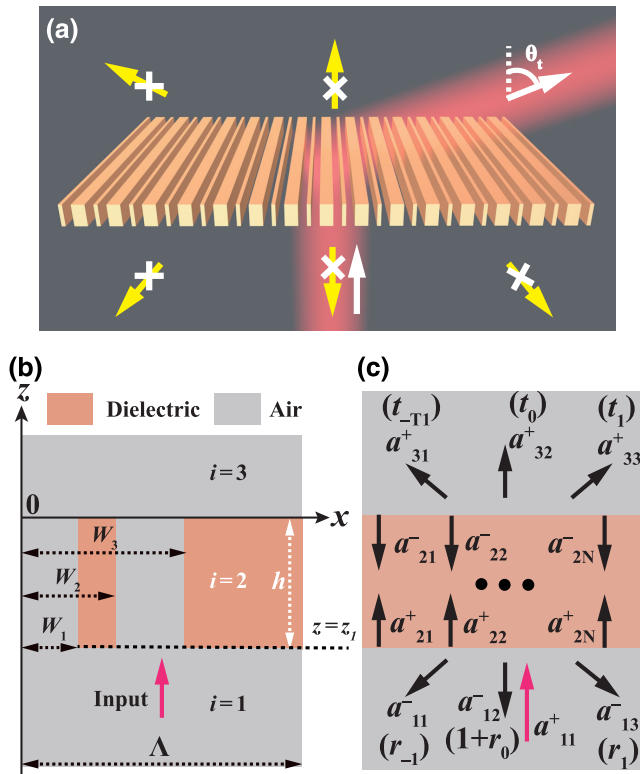
FIG. 1. (a) Schematic illustration of a monolayer dielectric metagrating for anomalous refraction through diffraction engineering. (b) Geometry of a grating period, composed of two asymmetric ridges. (c) Illustration of the waveguide modes bouncing inside the grating and the diffraction Bloch modes outside, which are coupled and matched at the top and bottom interfaces.

diffraction channels appear, and a phase-gradient meta-surface is a better choice. Here we focus on diffraction engineering of the three transmission channels and prohibiting the three reflection channels in order to achieve large-angle anomalous refraction and beam splitting at low THz frequencies.

To achieve this goal, we develop a simplified analytical model by expressing the electromagnetic fields inside and outside the metagrating as superpositions of plane-wave Bloch modes and connecting them via boundary conditions. By neglecting evanescent Bloch modes and keeping propagating ones, this model provides a clear physical interpretation of the conditions required to freely engineer diffraction in dielectric metagratings and inspires a design methodology in the case when the metagrating is made of a low-index dielectric. Evanescent modes can be safely ignored, as the skin depth is much smaller than the grating thickness. They do not communicate between layers. This model has been applied to explain the high reflectivity of high-contrast subwavelength gratings [49]. Here we extend it to analyze the diffraction behavior of dielectric

metagratings. The accuracy of such an analysis is checked further with full-wave simulations later.

In the monolayer metagrating shown in Fig. 1(b), the field distribution is divided into three layers (below, in, and above the grating). With TM-polarized excitation, the nonzero field components are E_x, H_y, and E_z. The fields in each layer can be written as a summation of Bloch modes as in Eqs. (2)–(4), with a periodicity of Λ:

$$
H_{yi}(x,z) = \sum_{m=1}^{M} h_{yim}(x)(a_{im}^{+}e^{-j\beta_{im}(z-z_i)} - a_{im}^{-}e^{j\beta_{im}(z-z_i)}),
$$
(2)

$$
E_{xi}(x,z) = \sum_{m=1}^{M} e_{xim}(x)(a_{im}^{+}e^{-j\beta_{im}(z-z_i)} + a_{im}^{-}e^{j\beta_{im}(z-z_i)}),
$$
(3)

$$
E_{zi}(x,z) = \sum_{m=1}^{M} e_{zim}(x)(a_{im}^{+}e^{-j\beta_{im}(z-z_i)} - a_{im}^{-}e^{j\beta_{im}(z-z_i)}).
$$
(4)

Here, i denotes the ith layer, as shown in Fig. 1(b); m is an integer index of the Bloch modes ranging from 1 to M, where M denotes the number of propagating Bloch modes in the ith layer, and evanescent modes are neglected. The rationality of the mode cutoff is discussed further in Sec. IV. z_i is the position of the top interface of the ith layer and is 0 for the last layer. The output of the grating is always located at $z = 0$. h_{yim}, e_{xim}, and e_{zim} are the lateral mode profiles, and a_{im}^{+} and a_{im}^{-} stand for the mode coefficients for forward and backward propagation in the ith layer in Fig. 1(c). β_{im} is the propagation constant of each Bloch mode along the z direction.

The lateral magnetic field profiles h_{yim} are given next, and the electric components e_{xim} and e_{zim} can be derived from Maxwell's equations, which are not shown for simplicity. For a homogeneous layer with relative permittivity $\epsilon_i = 1$, such as layers $i = 1, 3$ in Fig. 1(b), h_{yim} can be written as

$$
h_{yim}(x) = e^{-j(2\pi/\Lambda)mx},
$$
(5)

and β_{im} can be calculated from

$$
\beta_{im} = \sqrt{k_0^2 - \left(\frac{2\pi}{\Lambda}m\right)^2}.
$$
(6)

For an inhomogeneous grating layer, the lateral field profile is a waveguide mode propagating along z. h_{yim} can be

expressed in segments as

$$h_{yim}(0 < x < W_1) = A_m \cos\left[k_{am}\left(x - \frac{W_1}{2}\right)\right]$$
$$+ B_m \sin\left[k_{am}\left(x - \frac{W_1}{2}\right)\right], \quad (7)$$

$$h_{yim}(W_1 < x < W_2) = C_m \cos\left[k_{bm}\left(x - \frac{W_1 + W_2}{2}\right)\right]$$
$$+ D_m \sin\left[k_{bm}\left(x - \frac{W_1 + W_2}{2}\right)\right], \quad (8)$$

$$h_{yim}(W_2 < x < W_3) = E_m \cos\left[k_{am}\left(x - \frac{W_2 + W_3}{2}\right)\right]$$
$$+ F_m \sin\left[k_{am}\left(x - \frac{W_2 + W_3}{2}\right)\right], \quad (9)$$

$$h_{yim}(W_3 < x < \Lambda) = G_m \cos\left[k_{bm}\left(x - \frac{W_3 + \Lambda}{2}\right)\right]$$
$$+ H_m \sin\left[k_{bm}\left(x - \frac{W_3 + \Lambda}{2}\right)\right]. \quad (10)$$

When more ridges are included in a period, the lateral field profile can be expressed with additional segments. Here β_{im} is related to the lateral wave vectors k_{am} and k_{bm} by

$$\beta_{im} = \sqrt{k_0^2 - k_{am}^2} = \sqrt{\epsilon_d k_0^2 - k_{bm}^2}, \quad (11)$$

where ϵ_d is the relative permittivity of the dielectric ridge. h_{yim} and e_{zim} should be matched at $x = 0, W_1, W_2, W_3,$ and Λ as follows:

$$h_{yim}(\Lambda^-) = h_{yim}(0^+), \quad e_{zim}(\Lambda^-) = e_{zim}(0^+), \quad (12)$$
$$h_{yim}(W_1^-) = h_{yim}(W_1^+), \quad e_{zim}(W_1^-) = e_{zim}(W_1^+), \quad (13)$$
$$h_{yim}(W_2^-) = h_{yim}(W_2^+), \quad e_{zim}(W_2^-) = e_{zim}(W_2^+), \quad (14)$$
$$h_{yim}(W_3^-) = h_{yim}(W_3^+), \quad e_{zim}(W_3^-) = e_{zim}(W_3^+), \quad (15)$$

where the superscript minus and plus signs mean that the value is approached from the left and the right side, respectively. By combining Eqs. (11)–(15), one can write the coefficient matrix of the unknowns $A_m, B_m, \ldots, H_m$. The dispersion equation of the waveguide modes is obtained by setting the determinant of the coefficient matrix to zero; this is implicitly governed by $W_1, W_2, W_3,$ and Λ.

Having the lateral field profile, we next analyze the mode coefficients a_{im}^+ and a_{im}^- in each layer. a_{1m}^+ is known from the excitation, and a_{3m}^- is 0 as no reflection exists in the last layer. a_{1m}^- and a_{3m}^+ are the unknown diffraction

coefficients to be solved for on the reflection and transmission sides, and are finally determined by matching the tangential fields at the layer interfaces.

We call the Bloch modes diffraction modes in layers $i = 1, 3$, and waveguide modes in layer $i = 2$. Large-angle anomalous refraction limits the number of diffraction modes to $M = 3$ ($m = -1, 0, 1$), while the number of waveguide modes N is determined by the material and geometry of the metagrating. Matching the tangential fields at the layer interfaces gives the relation between the diffraction modes and waveguide modes, and the degree of freedom that governs this relation. Continuity of H_y at $z = 0$ leads to

$$\sum_{m=1}^{M} h_{y3m}(x) a_{3m}^+ = \sum_{n=1}^{N} h_{y2n}(x)(a_{2n}^+ - a_{2n}^-), \quad (16)$$

when M diffraction modes and N waveguide modes are supported in the third and second layer, respectively. Multiplying both sides by $h_{y3m}^* = e^{j(2\pi/\Lambda)mx}$ and taking the average over a period, we can write a_{3m}^+ explicitly as

$$a_{3m}^+ = \sum_{n=1}^{N} \frac{1}{\Lambda} \int_0^\Lambda h_{y2n}(x) h_{y3m}^*(x)\, dx (a_{2n}^+ - a_{2n}^-). \quad (17)$$

By writing the mode coefficients as a vector, such as $\vec{a}_3^+ = (a_{31}^+ \quad a_{32}^+ \quad \cdots \quad a_{3M}^+)^T$, Eq. (17) can be generalized to

$$\vec{a}_3^+ = H_{32}(\vec{a}_2^+ - \vec{a}_2^-), \quad (18a)$$
$$\vec{a}_3^+ = E_{32}(\vec{a}_2^+ + \vec{a}_2^-), \quad (18b)$$

where H_{32} (E_{32}) is the overlap integral matrix for the magnetic (electric) fields in the third and second layers. The matrix elements are defined purely by the lateral field profiles as

$$H_{32}(m, n) = \frac{1}{\Lambda} \int_0^\Lambda h_{y2n}(x) h_{y3m}^*(x)\, dx, \quad (19a)$$

$$E_{32}(m, n) = \frac{1}{\Lambda} \int_0^\Lambda e_{x2n}(x) e_{x3m}^*(x)\, dx. \quad (19b)$$

Further, we define a reflection matrix ρ_i relating the forward and backward mode coefficients by

$$\vec{a}_i^- = \rho_i \vec{a}_i^+, \quad (20)$$

so that Eq. (18) can be rewritten as

$$\vec{a}_3^+ = H_{32}(I - \rho_2)\vec{a}_2^+, \quad (21a)$$
$$\vec{a}_3^+ = E_{32}(I + \rho_2)\vec{a}_2^+. \quad (21b)$$
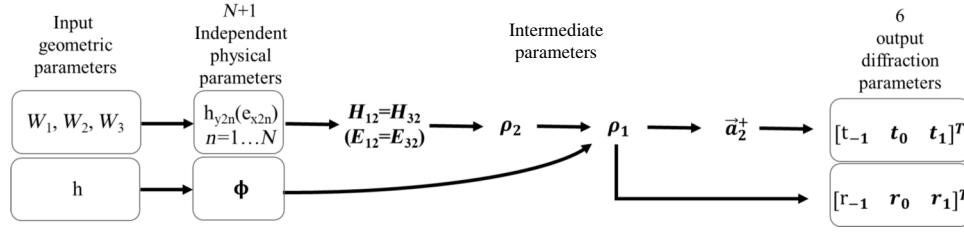
ρ_2 can be calculated from Eq. (21).

FIG. 2. Flowchart of the simplified analytical calculation of the diffraction coefficients from the geometric parameters for a monolayer metagrating.

Next, H_y and E_x are matched between the first and second layers at $z = -h$ as follows:

$$\vec{a}_1^+ - \vec{a}_1^- = (I - \rho_1)\vec{a}_1^+ = H_{12}(\phi^{-1} - \phi\rho_2)\vec{a}_2^+, \quad (22a)$$

$$\vec{a}_1^+ + \vec{a}_1^- = (I + \rho_1)\vec{a}_1^+ = E_{12}(\phi^{-1} + \phi\rho_2)\vec{a}_2^+, \quad (22b)$$

where $\phi = \mathrm{diag}[\exp(-j\beta_{2n}h)]$ is a diagonal matrix describing the accumulated phase factor when each waveguide mode propagates from $z = 0$ to $z = -h$.

In order to extract the diffraction coefficients a_{3m}^+ and a_{1m}^- (denoted by t_m and r_m for simplicity) from the given geometric parameters [W_1, W_2, W_3, h in Fig. 1(b)], we follow the flowchart in Fig. 2. Firstly, the lateral distributions h_{y2n} and e_{x2n} ($n = 1, \ldots, N$) of the waveguide modes in the grating layer are solved for from the width parameters (W_1, W_2, W_3) following Eqs. (7)–(15), while the lateral distributions of the diffraction modes in air ($h_{y1m} = h_{y3m}$, $e_{x1m} = e_{x3m}, m = -1, 0, 1$) are irrelevant to the geometry and are fixed as in Eq. (5). Hence all the overlap integral matrices H_{32}, H_{12}, E_{32}, and E_{12} are solved for following Eq. (19). Note that although each overlap integral matrix has $3 \times N$ elements, one cannot change each element independently. The definition in Eq. (19) shows that there are only N independent physical parameters ($h_{y21}, h_{y22}, \ldots, h_{y2N}$ or $e_{x21}, e_{x22}, \ldots, e_{x2N}$), which is the number of waveguide modes. And all four matrixes are totally determined by the N physical parameters. Then ρ_2 is solved for from Eq. (21) based on the above known quantities, and ρ_1 is solved for from Eq. (22) by introducing the thickness parameter h into the phase factor ϕ. From ρ_1, the diffraction coefficients $[r_{-1} \quad r_0 \quad r_1]^T$ ($\vec{a}_1^-$) are calculated. $\vec{a}_2^+$ is then solvable by revisiting Eq. (22), and finally the diffraction coefficients $[t_{-1} \quad t_0 \quad t_1]^T$ ($\vec{a}_3^+$) are obtained by revisiting Eq. (21). As indicated in Fig. 2, the input geometric parameters (W_1, W_2, W_3, h) are translated into independent physical parameters ($h_{y2n}, n = 1 \cdots N$, and ϕ). After intermediate calculations, they finally determine the output diffraction coefficients.

Following the flowchart, we define the calculation as a function with appropriate input and output parameters (geometric and diffraction parameters). Optimization of the grating geometry is done by minimizing an appropriately defined figure of merit (FOM) based on a gradient-descent algorithm. For large-angle refraction, the FOM is equal to $-|t_1|^2$, and for beam splitting into orders ± 1, the FOM is $\left||t_1|^2 - |t_{-1}|^2\right|/|t_1|^2$. The lower limit of the ridge width is set at 0.3 mm, considering the fabrication resolution of our current 3D printer. The thinnest possible structure is chosen to ensure light weight and compactness. The optimization implicitly helps to find the best grating geometry, in which the waveguide modes are constructively coupled into the desired diffraction order while they are destructively cancelled in other orders. All the metagratings considered throughout this paper are optimized following this rule in the simplified analytical model. However, their performance is verified with full-wave finite-difference time-domain (FDTD) simulations using the commercial software package Lumerical FDTD Solutions, and all the simulation results in the plots are from FDTD simulations for accuracy if not otherwise mentioned.

Figure 2 shows that the degrees of freedom in diffraction engineering are directly governed by the number of physical parameters (waveguide modes in the grating layer and the propagation phase factor), and indirectly related to the number of geometric parameters. Eventually, one needs a sufficient number of geometric parameters to control the waveguide modes and the diffraction. The number of physical parameters may not be equal to the number of geometric parameters, and the smaller of the two determines the degrees of freedom in diffraction engineering. Arbitrary control of the six diffraction parameters means six nonlinear constraints in the optimization problem. The conservation of power sets the last diffraction coefficient deterministically once the first five have been found. Accordingly, the minimum number of geometric and physical parameters should be five.

III. LIMITATIONS OF MONOLAYER LOW-INDEX METAGRATINGS

The grating material, the period, and the geometry of the constituent ridges together define the number of waveguide modes, the mode profiles, and the mode coefficients. We next show that the number of waveguide modes is determined mainly by the period and the refractive index rather than by the geometry of the grating ridges. When a
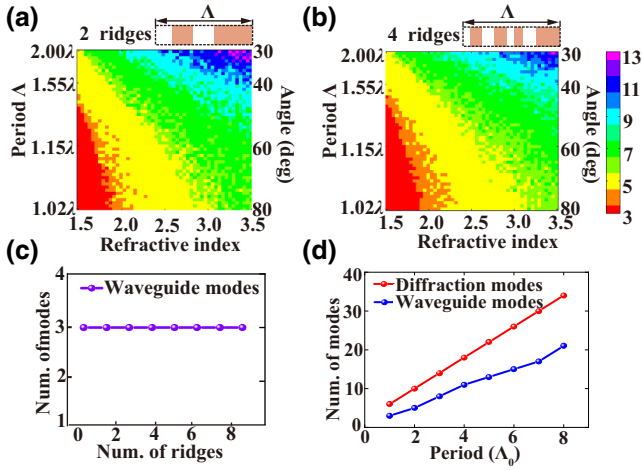
FIG. 3. (a),(b) Number of propagating waveguide modes in a monolayer dielectric grating for different refractive indices and periods (corresponding to different refraction angles on the right *y* axis) when (a) two random ridges and (b) four random ridges are included in a period. (c) Number of propagating waveguide modes in a PLA metagrating (refractive index 1.57) with a period of 1.02λ for $80°$ refraction when different numbers of ridges are included in a period. (d) Number of waveguide modes and diffraction modes when the grating period is an integer multiple of $\Lambda_0 = 1.02\lambda$ for higher-order diffraction engineering of monolayer PLA metagratings. All results are obtained from the simplified analytical model.

low-index dielectric (such as the polymer PLA at THz frequencies) is used, the number of waveguide modes in the metagrating is insufficient to fully control the diffraction pattern, leading to inefficient anomalous refraction.

Figures 3(a) and 3(b) summarize the number of waveguide modes N calculated from the simplified analytical model as functions of the period Λ (corresponding to different bending angles θ_t) and the refractive index, when the grating period contains two [Fig. 3(a)] or four [Fig. 3(b)] randomly distributed ridges. The similarity of the two figures demonstrates that N is insensitive to the detailed geometry of the grating, but is mainly determined by the refractive index and period. N decreases with decreasing period and refractive index.

When the refractive index is 3.5 (i.e., Si), N is not less than 5 for all bending angles up to $80°$, enough to control six diffraction coefficients. However, for a PLA grating with a refractive index of 1.57, N decreases from 6 to 3 as the period shrinks. Figure 3(c) shows that adding a greater number of ridges in a period (with a fixed $\Lambda = 1.02\lambda$ for $80°$ refraction) does not increase the number of waveguide modes, although this provides additional geometric parameters. Increasing the degrees of freedom is not feasible in a denser grating. Additionally, by increasing the grating period from Λ_0 to an integer multiple of Λ_0 (where $\Lambda_0 = \lambda / \sin 80°$), one can align the refraction with a higher diffraction order ($l > 1$) rather than the first
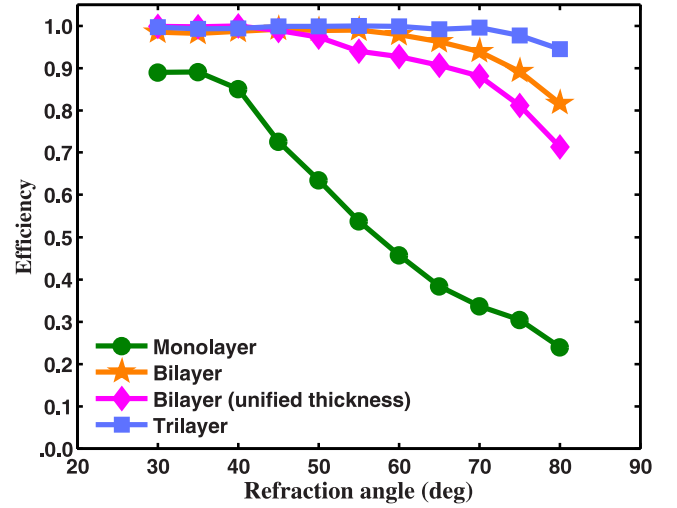

FIG. 4. Maximized first-order diffraction efficiency of monolayer (dots), bilayer (stars), and trilayer (squares) PLA metagratings for different refraction angles at 140 GHz. The efficiency of bilayer metagratings with unified thickness parameters for different refraction angles from $30°$ to $80°$ is added for comparison (diamonds).

order, following Eq. (1). Figure 3(d) shows the numbers of diffraction modes and waveguide modes in PLA gratings with different periods. The numbers of diffraction modes and waveguide modes increase simultaneously. One still does not have enough degrees of freedom to fully control the diffraction.

As a result, one can find a silicon bipartite grating composed of two ridges per period for $70°$ refraction, with an efficiency of 87% due to appropriate interaction of the five waveguide modes (the dimensions are given in Table I, row 1). In contrast, the efficiency of anomalous refraction drops with refraction angle for a bipartite PLA grating, as shown by the line of dots in Fig. 4, indicating an efficiency of 89% for $30°$ refraction (six waveguide modes) and only 24% for $80°$ refraction (three waveguide modes). The dimensions of the $30°$ and $80°$ PLA gratings are shown in Table I, in rows 2 and 3, respectively. These findings reveal the limitations of low-index metagratings for diffraction engineering due to the insufficient number of waveguide modes. Next we propose a solution to increasing the number of waveguide modes by using bilayer and multilayer configurations.

IV. BILAYER AND TRILAYER UNIFORM METAGRATINGS FOR ARBITRARY DIFFRACTION ENGINEERING

A. Large-angle anomalous refraction

Here we propose a bilayer uniform PLA metagrating [Fig. 5(a)] for large-angle anomalous refraction. The top and bottom PLA gratings, with only a single ridge in a

TABLE I. Geometric parameters of refracting and splitting metagratings with normal excitation.

	Material	Angle (deg)	Fig. No.	Λ (mm)	W_1 (mm)	W_2 (mm)	W_3 (mm)	h_1 (mm)	h_{sub1} (mm)	h_2 (mm)	h_{sub2} (mm)	h_3 (mm)	Efficiency η (%)	Bandwidth (90% of η) (%)
1	Si	70	1(b)	2.28	0.22	0.55	1.49	1.25	...	...	...	...	87	3
2	PLA	30	1(b)	4.28	0.62	1.64	3.73	3.98	...	...	...	...	89	...
3	PLA	80	1(b)	2.18	0.44	0.82	0.94	2.17	...	...	...	...	24	...
4	PLA	70	5(a)	2.28	1.36	0.77	...	2.04	3.59	5.76	...	...	94	7
5	PLA	80	5(a)	2.18	1.13	0.66	...	1.95	2.82	5.85	...	...	82	2
6	PLA	70	5(b)	2.28	1.72	1.06	0.58	2.23	1.48	2.50	2.39	2.39	99.5	7
7	PLA	80	5(b)	2.18	1.57	0.90	0.57	1.81	1.62	2.41	1.72	2.42	94	2
8	PLA	70	5(a)	2.28	1.14	0.52	...	2.00	2.10	3.10	...	...	88	21
9	PLA	80	5(a)	2.18	0.97	0.37	...	2.00	2.10	3.10	...	...	71	25
10	PLA	±70	5(a)	2.28	0.98	0.95	...	2.00	2.10	3.10	...	...	80	25

period, are separated by a uniform PLA slab. The field distribution is divided into five layers, as shown in Fig. 5(a). The simplified analytical model presented in Sec. II can be generalized to analyze multilayer grating configurations. The general field expressions are still given by Eqs. (2)–(4), where the lateral field profiles and dispersion relations of the waveguide modes are governed by matching of the boundary conditions at constant-x interfaces, and the forward and backward propagation coefficients along z can be derived by matching the boundary conditions at constant-z interfaces. Here we omit the details, and instead give a set of key equations governing the relation between the diffraction modes and waveguide modes as follows:

$$\vec{a}_5^+ = (t_{-1} \quad t_0 \quad t_1)^T = H_{54}(I - \rho_4)\vec{a}_4^+, \tag{23a}$$

$$\vec{a}_5^+ = (t_{-1} \quad t_0 \quad t_1)^T = E_{54}(I + \rho_4)\vec{a}_4^+, \tag{23b}$$

$$H_{34}(\phi_4^{-1} - \phi_4\rho_4)\vec{a}_4^+ = (I - \rho_3)\vec{a}_3^+, \tag{24a}$$

$$E_{34}(\phi_4^{-1} + \phi_4\rho_4)\vec{a}_4^+ = (I + \rho_3)\vec{a}_3^+, \tag{24b}$$

$$H_{32}(I - \rho_2)\vec{a}_2^+ = (\phi_3^{-1} - \phi_3\rho_3)\vec{a}_3^+, \tag{25a}$$

$$E_{32}(I + \rho_2)\vec{a}_2^+ = (\phi_3^{-1} + \phi_3\rho_3)\vec{a}_3^+, \tag{25b}$$

$$(I - \rho_1)\vec{a}_1^+ = (r_{-1} \quad 1 - r_0 \quad r_1)^T$$
$$= H_{12}(\phi_2^{-1} - \phi_2\rho_2)\vec{a}_2^+, \tag{26a}$$
$$(I + \rho_1)\vec{a}_1^+ = (r_{-1} \quad 1 + r_0 \quad r_1)^T$$
$$= E_{12}(\phi_2^{-1} + \phi_2\rho_2)\vec{a}_2^+. \tag{26b}$$

A flowchart for the analysis of a bilayer metagrating is shown in Fig. 6. The independent geometric parameters are $W_1, W_2, h_1, h_{sub}, h_2$. They are used to calculate $N + M + 3$ independent physical parameters: N waveguide modes in the bottom grating layer, M waveguide modes in the top grating layer, and three thickness-determined phase factors. From the analysis in Sec. III, $N = M \geq 3$ for low-index bilayer metagratings, and $N + M + 3$ is enough to control six diffraction coefficients. Given the input geometric parameters and related physical parameters, it is easy to conclude from Eqs. (23) and (26) that $[t_{-1} \quad t_0 \quad t_1]^T$ is mainly determined by the waveguide modes in the top grating layer, and $[r_{-1} \quad r_0 \quad r_1]^T$ by the bottom grating layer. Note that the modes in the top ($i = 4$) and bottom ($i = 2$) grating layers are not completely independent, and they still need to match the field in the middle layer
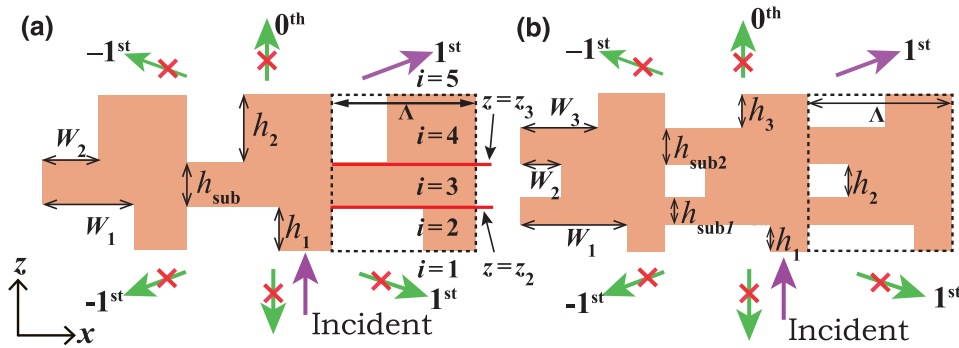

FIG. 5. Schematic illustration of (a) bilayer and (b) trilayer PLA metagrating. The dashed box depicts a period. The metagrating is composed of one ridge per period per layer, separated by uniform PLA slabs. To break the symmetry of the diffraction pattern, all the ridges are aligned with their right edges.
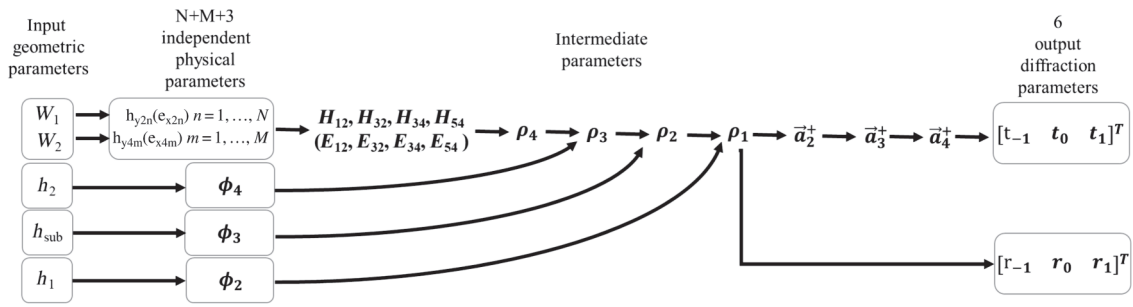
FIG. 6. Flowchart of simplified analytical calculation of diffraction coefficients from the geometric parameters of bilayer metagratings.

($i = 3$) at two interfaces ($z = z_2$ and $z = z_3$) following Eqs. (24) and (25). If the slab in the third layer is removed, the top and bottom waveguide modes experience stronger constraints since they have to be matched at the same interface. In contrast, such constraints are relaxed with an increased number of grating layers, and the waveguide modes in the first and last grating layers become more independent, allowing one to freely control the diffraction in transmission and reflection. We next show that the bilayer metagrating in Fig. 5(a) is already efficient for large-angle anomalous refraction, while the trilayer design in Fig. 5(b) offers near-perfect refraction.

We choose the minimum number of ridges in each grating layer, only one per period (uniform grating), to relax the fabrication requirements and to simplify the design process. The top and bottom ridges are forced to be aligned with their right edges. Such a sparse simple structure breaks two types of symmetry in a way necessary for efficient anomalous refraction: input and output symmetry along the $\pm z$ directions, and diffraction symmetry in the ± 1st orders. For a specific bending angle θ_t, the optimization is done to minimize the FOM $-|t_1|^2$. During each iteration, the FOM is evaluated following the flowchart in Fig. 6 with a given set of $[W_1, W_2, h_1, h_{sub}, h_3]$.

The efficiency of the optimized bilayer uniform PLA metagratings for different refraction angles is shown by the line of stars in Fig. 4, and is 94% and 82% for 70° and 80° refraction, respectively (the dimensions are given in Table I, rows 4 and 5). The bilayer design significantly improves the efficiency for large-angle refraction because of the increased number of waveguide modes. Because of the weak constraints on the waveguide modes in the top and bottom layers following Eqs. (24) and (25), the efficiency is not unity. In order to further improve the large-angle efficiency towards unity, trilayer designs (three layers of gratings separated by two slabs) are optimized [Fig. 5(b)], so that the top and bottom gratings gain more degrees of freedom to allow one to independently match the desired diffraction pattern in transmission and reflection. The efficiencies of the trilayer designs are 99.5% and 94% for 70°

and 80° refraction, respectively (the dimensions are given in Table I, rows 6 and 7).

An appropriate combination of different-angle metagratings may lead to more complicated devices for wavefront shaping such as tight-focusing lenses [33]. In order to keep a planar profile for further applications, we also investigate the bending efficiency when the thickness parameters are the same for all θ_t. To find a suitable set of unified thickness parameters for all refraction angles, the FOM for the optimization is defined as $-[|t_1(70°)|^2 + |t_1(75°)|^2 + |t_1(80°)|^2]$. The unified thickness parameters impose a restriction that leads to a decrease in efficiency beyond 50° (line of diamonds in Fig. 4). In the trilayer design, the geometric parameters are surplus, such that the unified thickness has no impact on the efficiency (not shown). In particular, we find that bilayer metagratings with the unified thickness sacrifice some efficiency but gain a wide bandwidth, as will be detailed later. To reconcile simplicity of structure, efficiency, and bandwidth performance, we finally choose bilayer metagratings with unified thickness parameters to achieve 70° and 80° refraction in the following simulation and experimental study (the dimensions are given in Table I, rows 8 and 9).

The efficiencies for all diffraction orders of the bilayer metagratings for 70° and 80° refraction at 140 GHz are shown in Fig. 7(a). The results from the simplified analytical model (SAM) and from FDTD simulations are in reasonably good agreement. Figure 7(b) depicts the field pattern of H_y in the optimized 80° metagratings calculated from the SAM and from FDTD simulations. The uniform wavefront indicates high diffraction efficiency towards the target direction. The magnitude is approximately $1/\sqrt{\cos 80°}$. The detailed near-field comparison between the SAM and FDTD simulations in Fig. 7(b) shows that the field above the grating is the same, while the field inside the grating shows some dissimilarity, especially around the layer interfaces. This indicates that evanescent modes inside the grating are indeed excited, but they decay so that they have negligible coupling with adjacent layers due to the large thickness, hardly contributing
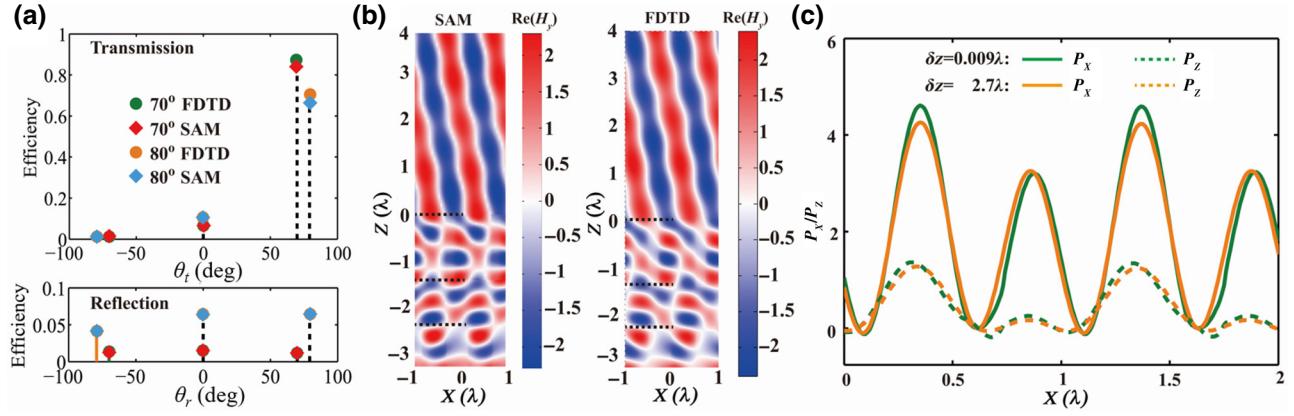
FIG. 7. (a) Efficiencies for all diffraction orders in transmission and reflection for optimized $70°$ and $80°$ refracting metagratings (with unified thickness for 140 GHz). The diamonds and circles show results from the SAM and from FDTD simulations, respectively, with reasonably good agreement. (b) Field distribution of H_y in $(-3.4\lambda < z < 0)$ and above the optimized $80°$ metagrating $(z > 0)$. The left and right panels are calculated from the SAM and from FDTD simulations, respectively. The dashed lines depict the interfaces between adjacent layers. (c) Poynting vector along x and z directions at the output interface and at 2.7λ away from the metagrating.

to the diffraction pattern outside the grating. To further validate the negligible contribution of the evanescent modes outside the grating, we plot the Poynting vector along the x and z directions (P_x and P_z) at two propagation distances in Fig. 7(c), one at the top interface and the other at 2.7λ away. One can safely ignore the evanescent diffraction modes, as the two P_x curves almost overlap, and so do the P_z curves.

Hence, the SAM solves the problem of the diffraction of the grating with enough accuracy, while offering a clear physical insight into the degrees of freedom for implementation of metagratings. In order to show clearly how the waveguide modes in a bilayer metagrating lead to efficient first-order diffraction in transmission, we simplify Eq. (23) further to

$$(t_{-1} \quad t_0 \quad t_1)^T = X\vec{a}_4^+, \qquad (27)$$

where $X = E_{54}(I + \rho_4)$ represents the coupling matrix between the diffraction modes and waveguide modes. Then each diffraction coefficient can be decomposed into three components as follows:

$$\begin{aligned} t_1 &= t_1^{(1)} + t_1^{(2)} + t_1^{(3)} \\ &= X_{(3,1)}a_{41}^+ + X_{(3,2)}a_{42}^+ + X_{(3,3)}a_{43}^+. \end{aligned} \qquad (28)$$

The remaining five diffraction coefficients can be written similarly as superpositions of three components. Figure 8 shows how the three components are superimposed (the three black arrows) in the final diffraction-coefficient vector (red arrows), with each part of the figure corresponding to a diffraction order of the optimized $70°$ refracting metagrating at 140 GHz. Evidently, the large magnitude of t_1 originates from the constructive superposition of the three waveguide modes in the top grating layer in

Fig. 8(a), while destructive superposition is observed in all the remaining parts of the figure, leading to very weak spurious diffraction. The parts of the figure are enlarged to different levels for clarity.

The frequency response of the first-order efficiency is plotted in Fig. 9(a) for $70°$ and $80°$ metagratings. When an efficiency above 90% of the maximum is considered [31,50], the bandwidth is 32 GHz, from 138 to 170 GHz, for $70°$ refraction, leading to a relative bandwidth of 21% (25% for $80°$ refraction). The beam direction can be scanned efficiently from $50.7°$ to $72.5°$ by changing the operation frequency. In contrast, currently reported metasurfaces and metagratings for large-angle refraction show a bandwidth of a few percent, as listed in Table II. Hence, the low-index metagrating proposed here is indeed a wideband anomalous refractor. To explain the bandwidth, the dispersion of each waveguide mode inside the $70°$ grating obtained from the SAM is plotted in Fig. 9(b). Below 177 GHz, there are three modes in the bottom grating (solid lines). The mode with the largest mode index is the fundamental mode. The cutoff frequencies (85 and 96 GHz) of the second and third modes are much less than the target frequency, 140 GHz. Hence, all three modes show very low dispersion behavior, and the same is true for the modes in the top layer (dashed lines). The higher-order modes with strong dispersion above 177 GHz are the main reason for efficiency deterioration, and set an upper limit on the operation frequency. The lower limit of the bandwidth originates from the cutoff of the first diffraction order. In fact, low dispersion and a wide bandwidth are unique merits of low-index metagratings. To prove this, we plot the bandwidth [Fig. 9(c)] and mode dispersion [Fig. 9(d)] of a high-index ($n = 3.5$) monolayer metagrating for $70°$ refraction at 140 GHz (Table I, row 1). The peak efficiency is 87%, but the bandwidth is much
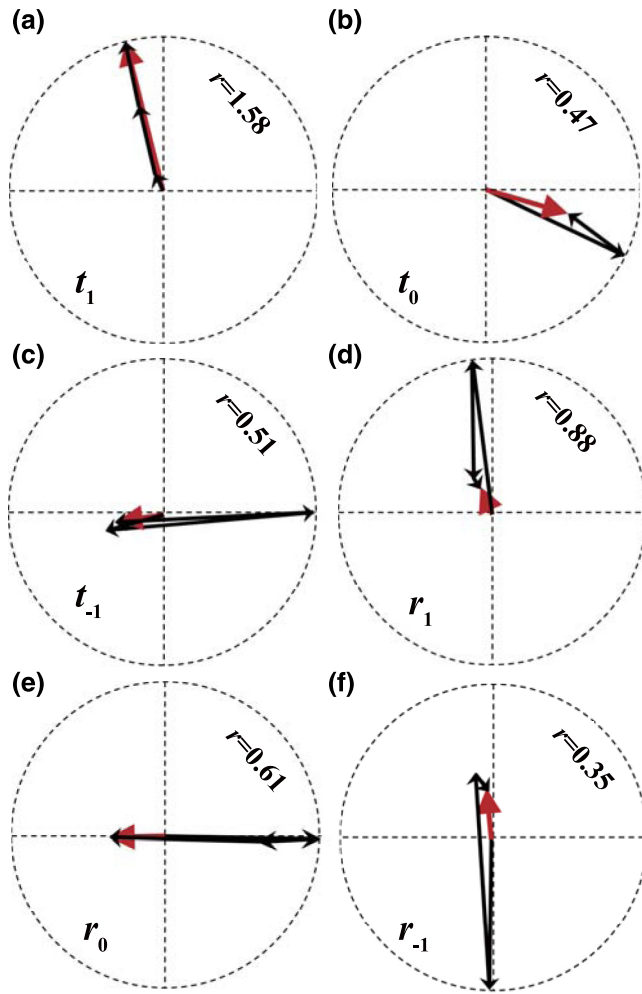
FIG. 8.   (a)–(c) Superposition of the three waveguide modes in the top grating layer in the diffraction-coefficient vector on the transmission side [t_1 (a), t_0 (b), and t_{-1} (c)]. (d)–(f) Superposition of the three waveguide modes in the bottom grating layer in the diffraction coefficients on the reflection side [r_1 (d), r_0 (e), and r_{-1} (f)]. Each part is obtained from the SAM and is enlarged to different levels for better comparison. The radius of each circle is added in the upper right corner.

narrower. Five waveguide modes in the grating layer show stronger dispersion, so that efficient first-order diffraction occurs tightly around the design frequency only.

B. Large-angle beam splitting

To further demonstrate the freedom of diffraction engineering in bilayer low-index metagratings, an efficient large-angle beam splitter is designed, which splits the incoming beam into −1st and +1st orders (±70° at 140 GHz) evenly, as shown in Fig. 10(a). The geometry of the bilayer metagrating is optimized in the analytical model with the aforementioned FOM $\left| |t_1|^2 - |t_{-1}|^2 \right| / |t_1|^2$ and the variables W_1 and W_2. The thickness parameters (h_1, h_2, h_{sub}) are still consistent with the previous refracting
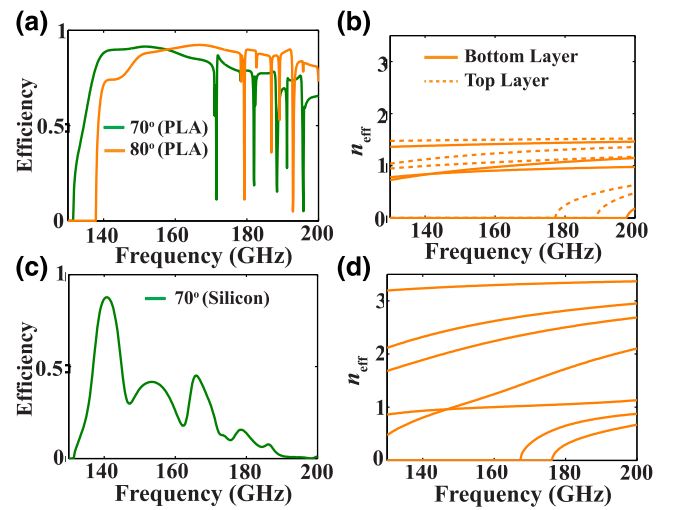

FIG. 9.   (a) Bandwidth for 70° and 80° anomalous refraction in PLA metagratings. (b) Mode dispersion $n_{eff} = \beta_i / k_0$ of waveguide modes in 70° metagrating. The solid lines depict the mode dispersion in the bottom layer, and the dashed lines for the top layer. (c) Bandwidth of a monolayer 70° refracting metagrating made of silicon. (d) Dispersion of five waveguide modes inside the monolayer silicon metagrating.

metasurfaces. The top and bottom ridges in the optimized bilayer metagrating have very similar widths due to the symmetry of the ±1st orders, but they have different thicknesses in order to match the input and output waves (the dimensions are given in Table I, row 10). The efficiency for each diffraction order at 140 GHz is shown in Fig. 10(b), with values of 40% for the ±1st orders and 3% for the zeroth order, and the rest of the energy is dominated by specular reflection.

The near-field distribution at 140 GHz is calculated from FDTD simulations and is shown in Fig. 10(c) for Gaussian beam illumination. One finds that the light propagates in extremely well-separated directions efficiently. Although it is designed for a single frequency, the bandwidth of the beam splitter is wide, as shown in Fig. 10(d). The diffraction efficiencies for the ±1st orders are equal from the cutoff frequency of 131.5 GHz to 150 GHz, and have a small difference up to 200 GHz except for an undesired resonance at 172.1 GHz in both diffraction orders. This beam splitter is efficient, with a wide bandwidth and a wide range of splitting angle tunable by frequency.

V. Experimental results

To experimentally validate the performance of the bilayer low-index metagrating, samples made of PLA for 70° refraction, 80° refraction, and ±70° splitting at 140 GHz are fabricated with a 3D printer (Raise 3D N2) using a fused-deposition modeling method. The nozzle diameter is 200 μm. The samples are built layer by layer along a uniform y direction. The temperatures of the supporting

TABLE II.   Summary of metasurfaces and metagratings for large-angle anomalous refraction.

Reference	θ_i/θ_t	Frequency	Material	Num. of elements per period	Min. feature size	Thickness	Efficiency η (%)	Bandwidth $(0.9 \times \eta)$ (%)
This work	0/70	140 GHz	PLA	2 vertically stacked	$\lambda/4$	3.4λ	Sim.: 88 Expt.: 82	21
This work	0/80	140 GHz	PLA	2 vertically stacked	$\lambda/5.5$	3.4λ	Sim.: 71 Expt.: 55	25
Ref. [16]	0/70	10.5 GHz	PCB	6	$\lambda/57$	$\lambda/9.4$	Sim.: 92.3 Expt.: 90.5	~ 3.3
Ref. [17]	0/71.8	20 GHz	PCB	10	$\lambda/197$	$\lambda/11$	Sim.: 67 (with loss) Expt.: 57.6	~ 2
Ref. [18]	0/80	10 GHz	PCB	6	$\lambda/150$	$\lambda/12$	Sim.: 76.6 (with loss) Expt.: 70	...
Ref. [19]	0/70	1 THz	PCB	4	...	...	Sim.: 91.4	~ 2
Ref. [30]	10/−70	20 GHz	PCB	3 vertically stacked	$\lambda/197$	$\lambda/1.8$	Sim.: 95.7	...
Ref. [31]	10/−60	20 GHz	PCB	2 above 2 below	$\lambda/10$	$\lambda/10$	Sim.: 89 Expt.: 90	~ 3
Ref. [32]	0/82	532 nm	TiO$_2$	1 (fishlike)	$\lambda/7.6$	$\lambda/1.7$	Sim.: 50 Expt.: ~ 40	~ 7
Ref. [33]	0/82	715 nm	Si	2	$\lambda/14.3$	$\lambda/2.9$	Expt.: 35 (p) Expt.: 32 (s)	~ 2.5
Ref. [34]	0/75	1050 nm	Si	1 (free-form)	$\lambda/14.2$	...	Sim.: 79 (TE) & 86 (TM) Expt.: 74 (TE) & 75 (TM)	~ 2.5
Ref. [35]	0/85	6.5 μm	Si	2	$\lambda/8.1$	$\lambda/1.78$	Sim.: 92	~ 0.6
Ref. [36]	0/65	650 nm	TiO$_2$	2	$\lambda/4.1$	$\lambda/1.9$	Sim.: 84	~ 16.7

base plate and printing nozzle are set to 60 °C and 215 °C, respectively. The printing speed has a constant value of 60 mm/s. A full view of the printed sample for 80° refraction is shown in Fig. 11(a); its size is 130 mm × 80 mm (61λ long and 37λ wide in terms of the design wavelength at 140 GHz). Enlarged top, bottom, and side views are included in the inset of Fig. 11(b).

The experimental setup is shown in Fig. 11(b). The source is a continuous-wave IMPATT diode with a frequency of 140 GHz. The beam is collimated by a Teflon convex lens with a focal length of 151 mm and a diameter of 4 inches. As the source is y-polarized, a 3D-printed half-wave plate [51] is used to convert the light into the x polarization so that one can measure the angular response in the horizontal plane. A polarizer is inserted between the sample and the HWP to further purify the polarization. A Schottky-diode detector is moved around the sample at a radius $R = 27$ cm (126λ away) with a step size of 2° to detect the far-field angular distribution of the diffracted light. A lock-in amplifier (Stanford Research System SR-830) [not shown in Fig. 11(b)] is connected to the laser and the detector for modulation and lock-in detection.

The intensity distribution of the beam without a metagrating is first measured and is shown as as the black curves in Fig. 12, which show a Gaussian-like intensity distribution centered at 0°. Then the diffracted intensities after the three metagratings are measured and are shown in Figs. 12(a)–12(c). All the results are normalized to the measured peak intensity of the source. The beam spot after collimation, with a beam waist of $r_b = 25$ mm, covers 23 periods. The finite beam width results in broadening of the diffraction over a certain angular range.

For better comparison of the simulation and experiment, the intensity distribution is simulated using two-dimensional FDTD simulations where the source is a Gaussian beam with a beam waist of 25 mm, as shown
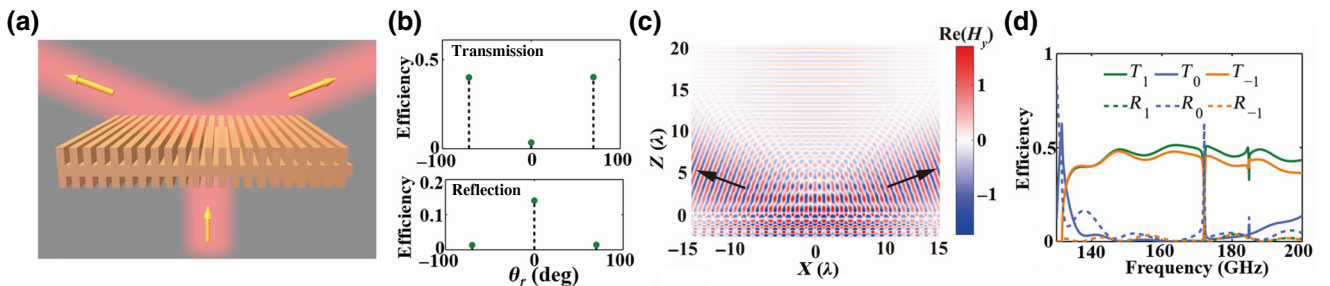

FIG. 10.   (a) Schematic illustration of a large-angle splitter (±70° at 140 GHz) made from a bilayer uniform PLA metagrating. (b) Simulated efficiency of each diffraction order at 140 GHz. (c) Field distribution (H_y) of the splitter with Gaussian beam excitation. (d) Bandwidth performance of each diffraction order. The results in (b)–(d) are from FDTD simulations.
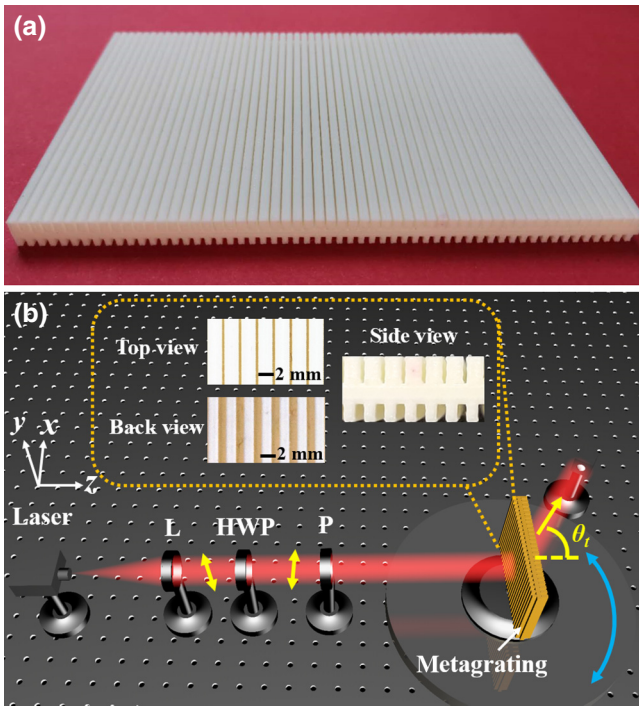
FIG. 11. (a) Full view of the 3D-printed PLA metagrating for 80° refraction. (b) Experimental setup for measuring the diffraction pattern of a metagrating. The inset depicts an enlarged top view, back view, and side view of the 80° metagrating. L, lens; HWP, half-wave plate; P, polarizer.

by the green curves in Fig. 12. The simulation domain is large enough to avoid edge effects. A perfectly-matched-layer boundary condition is applied in all directions. A linear monitor is placed 0.14λ after the sample to detect electromagnetic components, and then a near-to-far transformation is implemented to obtain the angular distribution at a distance of 27 cm, which is consistent with the experimental configuration.

For 70° refraction, the measured peak is located at 72°, with little difference compared with the design and the simulation result. For 80° refraction, the position of the

intensity peak agrees well with the design. We next calculate the diffraction efficiency for the first order while taking into account the beam-broadening effect. The input power is obtained by integration of the source intensity from −90° to 90°. The power diffracted into the desired direction is integrated from null to null (around −25 dB). The refraction efficiency is defined as the power in the desired diffraction order over the incident power [17,18], and is a total efficiency taking reflection and absorption into account. The measured efficiencies are 82% and 55% for 70° and 80° refraction, respectively. The simulated efficiencies are similarly calculated as 85% and 61%. The experimental and simulation results generally agree, with a slight difference due to fabrication errors. The efficiency degradation as compared with the case of an infinite-period grating [88% and 71% for 70° and 80° refraction, respectively, in Fig. 7(a)] is due to the finite illumination area. Taking 80° refraction as an example, the simulated efficiency is 67% if a Gaussian beam with a beam waist of 44 mm is used, and 70% with a beam waist of 85 mm, gradually approaching the theoretical limit of 71%. Therefore, by increasing the beam size and the sample size, one can match the measured efficiency better to the theoretical prediction. As the source frequency cannot be tuned, the bandwidth performance is not yet measured.

For the 70° splitter, the experimental results agree well with the simulations shown in Fig. 12(c). The measured peaks lie between −72° and +72° at the working frequency of 140 GHz. The measured efficiencies are 40% for both the −1st and the first order, and their total is 80% of the input power. The simulated total diffraction efficiency is 80% as well.

VI. Discussion and conclusion

We compare our low-index metagratings with existing large-angle refracting metasurfaces and metagratings in Table II from different points of view. The layered PCB metagratings described in Refs. [30,31] and the layered dielectric metagratings here show some similarity in
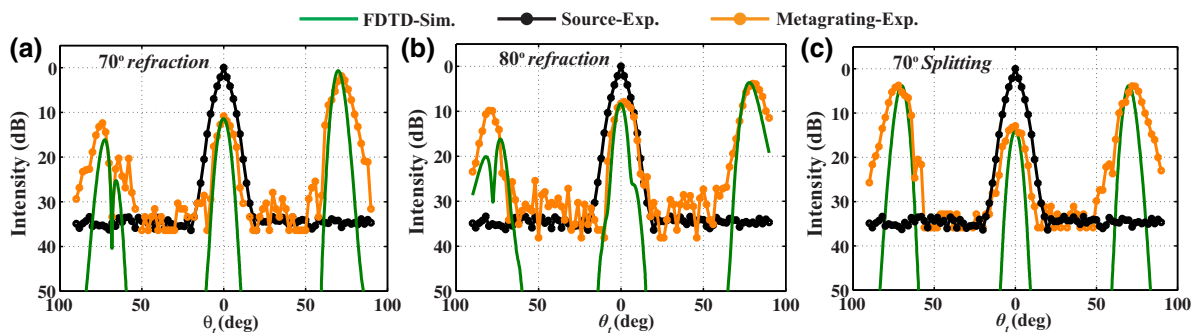

FIG. 12. Measured and simulated angular intensity distributions for different metagratings at 140 GHz. (a) 70° refraction, (b) 80° refraction, (c) ±70° splitting. The measured intensity distribution of the source is superimposed on each plot for comparison.

their structure, both requiring asymmetry among the layers so as to match the different wave impedances of the input and output waves. To achieve the same functionality, the PCB structures are designed to implement the desired impedance sheets, and the dielectric metagratings are designed to implement the desired waveguide modes in the grating layer, with an experimental demonstration at THz frequencies. The choice of a low-index dielectric and the 3D-printing fabrication method avoid the challenges that arise when microwave and visible solutions are scaled to the THz range (insufficient PCB resolution and limited etching depth in microfabrication and nanofabrication techniques). References [16–19] describe metasurfaces with more elements in a period to implement continuous impedance profiles, while the rest can be classified as metagratings with a smaller number of elements per period for diffraction engineering. Our design is among those with the most sparse element distribution, leading to a minimum feature size of around $\lambda/5$, which relaxes the fabrication requirements and promises applications at higher THz frequencies. Our metagratings show a relatively high efficiency among the reported results as they do not incur strong reflection and absorption, due to the low index and low loss. In term of bandwidth (90% of maximum), PCB elements relying on *LC* resonances are inherently narrowband. Increased mode dispersion places restrictions on the bandwidth of the high-index dielectric scatterers described in Refs. [33–36]. The low-index design here is indeed wide-band, benefiting from a low mode dispersion. The drawback is that it is much thicker than other designs (PCB metasurfaces can be as thin as $\lambda/10$).

To summarize, we derive from a simplified analytical model the result that the number of waveguide modes inside a metagrating is a key factor governing diffraction. A low-index dielectric metagrating with a refractive index of 1.57, suitable for 3D printing and for terahertz applications, shows limited capability for diffraction control due to an insufficient number of waveguide modes. Bilayer and trilayer metagratings with only one ridge per period per layer are proposed in order to enrich the waveguide modes and to gain enough degrees of freedom for efficient large-angle anomalous refraction and beam splitting. Because of the low dispersion of the waveguide modes in the ridges of the low-index gratings, such diffraction engineering is wide-band, with a simulated relative bandwidth of 21% for $70°$ refraction. To demonstrate this methodology, metagratings for $70°$ refraction, $80°$ refraction, and $\pm70°$ splitting are 3D printed and tested at 140 GHz, with measured efficiencies of 82%, 55%, and 80%, respectively, consistent with simulations with negligible material loss. Therefore, the proposed bilayer low-index metagratings, with a simple configuration and low-cost fabrication, show great flexibility in beam-direction control and are well suited for challenging THz applications.

[1] H.-T. Chen, A. J. Taylor, and N. Yu, A review of metasurfaces: Physics and applications, Rep. Prog. Phys. **79,** 076401 (2016).

[2] Q. He, S. Sun, S. Xiao, and L. Zhou, High-efficiency metasurfaces: Principles, realizations, and applications, Adv. Opt. Mater. **6,** 1800415 (2018).

[3] N. Yu, P. Genevet, M. A. Kats, F. Aieta, J.-P. Tetienne, F. Capasso, and Z. Gaburro, Light propagation with phase discontinuities: Generalized laws of reflection and refraction, Science **334,** 333 (2011).

[4] S. Sun, K.-Y. Yang, C.-M. Wang, T.-K. Juan, W. T. Chen, C. Y. Liao, Q. He, S. Xiao, W.-T. Kung, G.-Y. Guo, Z. Lei, and T. D. Ping, High-efficiency broadband anomalous reflection by gradient meta-surfaces, Nano Lett. **12,** 6223 (2012).

[5] H. Zhang, X. Zhang, Q. Xu, Q. Wang, Y. Xu, M. Wei, Y. Li, J. Gu, Z. Tian, C. Ouyang, X. Zhang, C. Hu, J. Han, and W. Zhang, Polarization-independent all-silicon dielectric metasurfaces in the terahertz regime, Photon. Res. **6,** 24 (2018).

[6] A. Epstein and G. V. Eleftheriades, Passive lossless huygens metasurfaces for conversion of arbitrary source field to directive radiation, IEEE Trans. Antennas Propag. **62,** 5680 (2014).

[7] V. S. Asadchy, M. Albooyeh, S. N. Tcvetkova, A. Díaz-Rubio, Y. Ra'di, and S. Tretyakov, Perfect control of reflection and refraction using spatially dispersive metasurfaces, Phy. Rev. B **94,** 075142 (2016).

[8] N. Mohammadi Estakhri and A. Alù, Wave-Front Transformation with Gradient Metasurfaces, Phys. Rev. X **6,** 041008 (2016).

[9] A. Epstein and G. V. Eleftheriades, Synthesis of Passive Lossless Metasurfaces Using Auxiliary Fields for Reflectionless Beam Splitting and Perfect Reflection, Phys. Rev. Lett. **117,** 256103 (2016).

[10] D.-H. Kwon, Lossless scalar metasurfaces for anomalous reflection based on efficient surface field optimization, IEEE Antennas Wirel. Propag. Lett. **17,** 1149 (2018).

[11] A. Díaz-Rubio, V. S. Asadchy, A. Elsakka, and S. A. Tretyakov, From the generalized reflection law to the realization of perfect anomalous reflectors, Sci. Adv. **3,** e1602714 (2017).

[12] V. S. Asadchy, A. Wickberg, A. Díaz-Rubio, and M. Wegener, Eliminating scattering loss in anomalously reflecting optical metasurfaces, ACS Photonics **4,** 1264 (2017).

[13] A. Díaz-Rubio, J. Li, C. Shen, S. A. Cummer, and S. A. Tretyakov, Power flow–conformal metamirrors for engineering wave reflections, Sci. Adv. **5,** eaau7288 (2019).

[14] J. P. Wong, A. Epstein, and G. V. Eleftheriades, Reflectionless wide-angle refracting metasurfaces, IEEE Antennas Wirel. Propag. Lett. **15,** 1293 (2016).

[15] A. Epstein and G. V. Eleftheriades, Arbitrary power-conserving field transformations with passive lossless omega-type bianisotropic metasurfaces, IEEE Trans. Antennas Propag. **64,** 3880 (2016).

[16] G. Lavigne, K. Achouri, V. S. Asadchy, S. A. Tretyakov, and C. Caloz, Susceptibility derivation and experimental demonstration of refracting metasurfaces without spurious diffraction, IEEE Trans. Antennas Propag. **66,** 1321 (2018).

[17] M. Chen, E. Abdo-Sánchez, A. Epstein, and G. V. Eleftheriades, Theory, design, and experimental verification of a reflectionless bianisotropic Huygens' metasurface for wide-angle refraction, Phys. Rev. B **97,** 125433 (2018).

[18] G. Xu, S. V. Hum, and G. V. Eleftheriades, Augmented Huygens' metasurfaces employing baffles for precise control of wave transformations, IEEE Trans. Antennas Propag. **67,** 6935 (2019).

[19] M. A. Cole, A. Lamprianidis, I. V. Shadrivov, and D. A. Powell, Refraction efficiency of Huygens' and bianisotropic terahertz metasurfaces, arXiv:1812.04725 (2018).

[20] Y. Ra'di, D. L. Sounas, and A. Alù, Metagratings: Beyond the Limits of Graded Metasurfaces for Wave Front Control, Phys. Rev. Lett. **119,** 067404 (2017).

[21] H. Chalabi, Y. Ra'di, D. Sounas, and A. Alù, Efficient anomalous reflection through near-field interactions in metasurfaces, Phys. Rev. B **96,** 075432 (2017).

[22] M. Memarian, X. Li, Y. Morimoto, and T. Itoh, Wideband/angle blazed surfaces using multiple coupled blazing resonances, Sci. Rep. **7,** 42286 (2017).

[23] A. M. Wong and G. V. Eleftheriades, Perfect Anomalous Reflection with a Bipartite Huygens' Metasurface, Phys. Rev. X **8,** 011036 (2018).

[24] O. Rabinovich and A. Epstein, Analytical design of printed circuit board (PCB) metagratings for perfect anomalous reflection, IEEE Trans. Antennas Propag. **66,** 4086 (2018).

[25] Z.-L. Deng, S. Zhang, and G. P. Wang, A facile grating approach towards broadband, wide-angle and high-efficiency holographic metasurfaces, Nanoscale **8,** 1588 (2016).

[26] X. Dong, J. Cheng, F. Fan, and S. Chang, Low-index second-order metagratings for large-angle anomalous reflection, Opt. Lett. **44,** 939 (2019).

[27] X. Dong, J. Cheng, F. Fan, Z. Zhang, Y. Liu, X. Wang, and S. Chang, Extremely large-angle beam deflection based on low-index sparse dielectric metagratings, J. Phys. D: Appl. Phys. **53,** 245101 (2020).

[28] V. Popov, F. Boust, and S. N. Burokur, Controlling Diffraction Patterns with Metagratings, Phys. Rev. Appl. **10,** 011002 (2018).

[29] V. Popov, F. Boust, and S. N. Burokur, Constructing the near Field and far Field with Reactive Metagratings: Study on the Degrees of Freedom, Phys. Rev. Appl. **11,** 024074 (2019).

[30] A. Epstein and O. Rabinovich, in *Proceedings of the 12th European Conference on Antennas and Propagation (EuCAP 2018)* (IEEE, London, UK, 2018), p. 2046.

[31] O. Rabinovich and A. Epstein, Arbitrary diffraction engineering with multilayered multielement metagratings, IEEE Trans. Antennas Propag. **68,** 1553 (2020).

[32] E. Khaidarov, H. Hao, R. Paniagua-Domínguez, Y. F. Yu, Y. H. Fu, V. Valuckas, S. L. K. Yap, Y. T. Toh, J. S. K. Ng, and A. I. Kuznetsov, Asymmetric nanoantennas for ultra-high angle broadband visible light bending, Nano Lett. **17,** 6267 (2017).

[33] R. Paniagua-Dominguez, Y. F. Yu, E. Khaidarov, S. Choi, V. Leong, R. M. Bakker, X. Liang, Y. H. Fu, V. Valuckas, L. A. Krivitsky, and A. I. Kuznetsov, A metalens with a near-unity numerical aperture, Nano Lett. **18,** 2124 (2018).

[34] D. Sell, J. Yang, S. Doshay, R. Yang, and J. A. Fan, Large-angle, multifunctional metagratings based on freeform multimode geometries, Nano Lett. **17,** 3752 (2017).

[35] Z. Fan, M. R. Shcherbakov, M. Allen, J. Allen, B. Wenner, and G. Shvets, Perfect diffraction with multiresonant bianisotropic metagratings, ACS Photonics **5,** 4303 (2018).

[36] Tan Shi, Yujie Wang, Zi-Lan Deng, Xuan Ye, Zhenxing Dai, Yaoyu Cao, Bai-Ou Guan, Shumin Xiao, and Xiangping Li, All-dielectric kissing-dimer metagratings for asymmetric high diffraction, Adv. Opt. Mater. **7,** 1901389 (2019).

[37] C. Pfeiffer and A. Grbic, Bianisotropic Metasurfaces for Optimal Polarization Control: Analysis and Synthesis, Phys. Rev. Appl. **2,** 044011 (2014).

[38] Y. Kasahara, A. Alù, M. Wu, K. Kosaka, H. Toyao, and E. Hankui, in *2018 IEEE International Symposium on Antennas and Propagation and USNC/URSI National Radio Science Meeting* (IEEE, Boston, Massachusetts, USA, 2018) p. 521.

[39] P. D. Cunningham, N. N. Valdes, F. A. Vallejo, L. M. Hayden, B. Polishak, X.-H. Zhou, J. Luo, A. K.-Y. Jen, J. C. Williams, and R. J. Twieg, Broadband terahertz characterization of the refractive index and absorption of some important polymeric and organic electro-optic materials, J. Appl. Phys. **109,** 043505 (2011).

[40] S. Busch, M. Weidenbach, M. Fey, F. Schäfer, T. Probst, and M. Koch, Optical properties of 3D printable plastic in the THz regime and their application for 3D printed THz optics, J. Infrared Millim. Terahertz Waves **35,** 993 (2014).

[41] R. T. Ako, A. Upadhyay, W. Withayachumnankul, M. Bhaskaran, and S. Sriram, Dielectrics for terahertz metasurfaces: Material selection and fabrication techniques, Adv. Opt. Mater. **8,** 1900750 (2020).

[42] F. Zhou, W. Cao, B. Dong, T. Reissman, W. Zhang, and C. Sun, Additive manufacturing of a 3D terahertz gradient-refractive index lens, Adv. Opt. Mater. **4,** 1034 (2016).

[43] J. Sun and F. Hu, Three-dimensional printing technologies for terahertz applications: A review, Int. J. RF Microw. Comput.-Aided Eng. **30,** e21983 (2020).

[44] J. F. Federici, B. Schulkin, F. Huang, D. Gary, R. Barat, F. Oliveira, and D. Zimdars, THz imaging and sensing for security applications–explosives, weapons and drugs, Semicond. Sci. Tech. **20,** S266 (2005).

[45] K. Kawase, T. Shibuya, S. Hayashi, and K. Suizu, THz imaging techniques for nondestructive inspections, C. R. Phys. **11,** 510 (2010).

[46] R. Zhou, C. Wang, W. Xu, and L. Xie, Biological applications of terahertz technology based on nanomaterials and nanostructures, Nanoscale **11,** 3445 (2019).

[47] P. S. J. Russell, Optics of Floquet-Bloch waves in dielectric gratings, Appl. Phys. B **39,** 231 (1986).

[48] E. G. Loewen and E. Popov, *Diffraction Gratings and Applications* (CRC Press, Boca Raton, FL, 1997).

[49] V. Karagodsky, F. G. Sedgwick, and C. J. Chang-Hasnain, Theoretical analysis of subwavelength high

contrast grating reflectors, Opt. Express **18,** 16973 (2010).

[50] O. Rabinovich, I. Kaplon, J. Reis, and A. Epstein, Experimental demonstration and in-depth investigation of analytically designed anomalous reflection metagratings, Phys. Rev. B **99,** 125101 (2019).

[51] X.-P. Dong, J.-R. Cheng, F. Fan, S.-T. Xu, X.-H. Wang, and S.-J. Chang, Wideband sub-THz half-wave plate using 3D-printed low-index metagratings with superwavelength lattice, Opt. Express **27,** 202 (2019).